



**Vertically Oriented TiS<sub>2</sub>-x Nanobelt Arrays as Binder- and Carbon-Free Intercalation Electrodes for Li- and Na- based Energy Storage Devices**

Journal:	<i>Journal of Materials Chemistry A</i>
Manuscript ID	TA-ART-06-2018-005645.R1
Article Type:	Paper
Date Submitted by the Author:	19-Jul-2018
Complete List of Authors:	Hawkins, Casey; University of Utah, Chemistry Whittaker-Brooks, Luisa; University of Utah, Chemistry

SCHOLARONE™  
Manuscripts



Journal Name

ARTICLE

## Vertically Oriented $\text{TiS}_{2-x}$ Nanobelt Arrays as Binder- and Carbon-Free Intercalation Electrodes for Li- and Na- based Energy Storage Devices

Received 00th January 20xx,  
Accepted 00th January 20xx

DOI: 10.1039/x0xx00000x

www.rsc.org/

Casey G. Hawkins<sup>a</sup> and Luisa Whittaker-Brooks<sup>a,\*</sup>

Titanium (IV) sulfide ( $\text{TiS}_2$ ) is a promising 2D layered material for energy storage applications. However, its electrochemical performance has been hindered by its low ion diffusion coefficient and inconsistencies determining its electrical properties. To overcome these challenges, bulk  $\text{TiS}_2$  cathodes are normally mixed with conductive additives (typically carbon) and polymer binders (typically polyvinylidene fluoride –PVDF) to yield a paste that is subsequently cast onto a current collector. The electrochemical performance of the electrode is lowered due to the extra weight of all the inactive components (i.e., additives, polymer binder, and metal substrates) introduced during the fabrication process. An alternative to the use of pasted electrodes is the direct growth of well-defined nanostructures on a conducting substrate. In this study, we report the synthesis, characterization, and electrochemical performance of carbon- and binder-free cathodes comprising highly conducting  $\text{TiS}_2$  nanobelts. The fabricated  $\text{TiS}_2$  nanobelts are highly anisotropic and are vertically grown directly on the current collector to yield a spatially controlled array. The short ion diffusion paths, high electrical conductivity and absence of additives that hinder ion migration lead to Li- and Na- based  $\text{TiS}_2$  electrochemical devices exhibiting high specific capacity, less capacity fade, and resilience under higher cycling rates. We also present the effects of sulfur vacancies on the electrochemical performance of both vertically oriented Li- and Na- based  $\text{TiS}_{2-x}$  nanobelt array cathode insertion hosts. It is also worth mentioning that Na-ion half-cells comprising our vertically oriented  $\text{TiS}_2$  nanobelt arrays exhibit a discharge capacity of 217 mAh  $\text{g}^{-1}$  (theoretical specific capacity of 239 mAh  $\text{g}^{-1}$ ). This discharge capacity equates to 0.91 Na per  $\text{TiS}_2$  unit –exceeding the maximum loading ever obtained of 0.8 Na per  $\text{TiS}_2$  under practical operation. We thus observe that scaling to finite sizes as well as fabricating highly anisotropic nanobelt arrays are found to profoundly alter both the kinetics of Li- and Na- ion insertion and the electrochemical performance of  $\text{TiS}_2$ .

### Introduction

With the dramatic increase of portable electronics, the demand for pure or hybrid electric vehicles, and the need for grid-scale energy storage for renewable energy technologies, there is an urgent necessity to develop rechargeable energy storage technologies with high energy density, high power density, and long-life cycles. Rechargeable energy storage technologies such as lithium (Li)-ion batteries have become the most widely implemented platform since commercialized in the early 1990s.<sup>1, 2</sup> While Li-ion batteries have dominated the rechargeable energy storage market, there are several

hurdles currently hindering their widespread use in electric vehicles and in grid-scale electrical storage devices.<sup>3</sup> One primary hurdle pertains to safety issues presented by using Li and flammable organic electrolytes. Even if these safety issues are resolved, due to the limited number of Li deposits globally, there are concerns that Li is not a sustainable resource.<sup>3, 4</sup> Forecasting the energy storage landscape for Li-ion technologies, their high demand, and the limited supply of Li sources may increase their cost and jeopardize their further development.

Several ions such as monovalent sodium ( $\text{Na}^+$ ) and potassium ( $\text{K}^+$ ),<sup>5-10</sup> bivalent magnesium ( $\text{Mg}^{2+}$ ) and calcium ( $\text{Ca}^{2+}$ ),<sup>11-14</sup> and trivalent aluminum ( $\text{Al}^{3+}$ ),<sup>15-18</sup> have been investigated as possible alternatives to  $\text{Li}^+$ .  $\text{Na}^+$  is an attractive candidate due to its relative earth abundance as well as the widespread availability of Na sources around the globe. The stark similarity between the  $\text{Na}^+$  and  $\text{Li}^+$  ions in

<sup>a</sup> Department of Chemistry, University of Utah, 315 South 1400 East, Rm 2020, Salt Lake City, Utah, 84112, USA. \*Email: [luisa.whittaker@utah.edu](mailto:luisa.whittaker@utah.edu)

terms of their physical and chemical properties allows for a “lithium-like approach” where most of the research advancements obtained with Li-ion technologies may be fully adaptable to Na-ion technologies. Shifting to Na-ion energy storage technologies may still require the development of efficient cathode and anode materials that can overcome the sluggish kinetics of the Na<sup>+</sup> intercalation/de-intercalation reaction caused by the relatively larger ionic radius of Na<sup>+</sup> (102 pm) versus Li<sup>+</sup> (76 pm).<sup>19-21</sup> Various layered metal oxides,<sup>22-26</sup> phosphates/fluorophosphates,<sup>27-29</sup> metal fluorides,<sup>30-32</sup> and metal chalcogenides<sup>33-37</sup> have been developed as reversible intercalation/de-intercalation cathodes for Na-ion energy storage devices. However, most of these potential electrode materials suffer from limited specific capacities and rate capabilities. Among these materials, metal chalcogenides have drawn significant interests because of their promise of overcoming these limitations due to their high electrical conductivity, large interlamellar spacing, and short ion/charge diffusion paths. As an archetypal layered metal chalcogenide, titanium (IV) sulfide (TiS<sub>2</sub>) possesses several properties that are advantageous for energy storage applications such as earth abundance, high electrical conductivity (10<sup>4</sup> S m<sup>-1</sup>), and higher theoretical specific capacity (239 mAh g<sup>-1</sup>) than that of the structurally limited specific capacity for commercially ubiquitous LiCoO<sub>2</sub> (140 mAh g<sup>-1</sup>, when cycled between 3.0 – 4.5 V).<sup>38,39</sup>

TiS<sub>2</sub> crystallizes in a simple hexagonal structure comprising layers of [TiS<sub>6</sub>] octahedra sharing edges and corners. The layers are weakly bound by van der Waals' electrostatic forces along the *c*-axis and the spacing between the layers (5.69 Å) provides abundant sites for the intercalation/de-intercalation of organic and inorganic guest species.<sup>40-45</sup> In the mid-1970s, Whittingham first demonstrated the possibility of using metallic lithium, coupled with a TiS<sub>2</sub> single-crystal as a viable secondary energy storage material.<sup>46</sup> While using a single-crystal provides key fundamental insight into the properties of TiS<sub>2</sub>, this is not a practical synthesis that would allow commercialization on any appreciable scale. Correspondingly, in the late 1970s and early 1980s, Whittingham, Newman, and Klemann also investigated the electrochemical properties of TiS<sub>2</sub> as a possible intercalation host for Na-ions.<sup>46,47</sup> Both reports indicate that TiS<sub>2</sub> would not be suitable as a cathode due the loading of Na<sup>+</sup> to be limited to *x* = 0.8 for Na<sub>*x*</sub>TiS<sub>2</sub>. Additionally, a potential phase change in the TiS<sub>2</sub> crystal structure was observed upon insertion and de-insertion of Na<sup>+</sup> ions that results in unrecoverable capacity loss.<sup>47</sup> Nonetheless, a recent study has shown that the size of the TiS<sub>2</sub> crystallites has an impact on the stability and Na-ion loading. Through a colloid synthesis route, Liu *et al.* fabricated TiS<sub>2</sub> nanoplatelets with diameters of 100–200 nm and thicknesses around 5 nm. Batteries employing these nanoplatelets exhibit high Na-ion loading (186 mAh g<sup>-1</sup>) and good cycling stability (76 % capacity retention after 300 cycles at a 2 C rate).<sup>48</sup>

The solid-state synthesis of TiS<sub>2</sub> from elemental Ti and S typically yields micron-sized hexagonal platelets. As these platelets are free-flowing, a polymeric binder, typically polyvinylidene fluoride (PVDF), is used to create a slurry that is tape-cast onto a current collector. Since PVDF is an insulator, conductive carbon is usually added to the slurry to overcome its low electrical conductivity. While the addition of conductivity enhancers (additives) is the current procedure used to overcome the low conductivity of oxide-based cathode materials such as LiCoO<sub>2</sub>, Li<sub>1-x</sub>Mn<sub>2</sub>O<sub>4</sub> and LiFePO<sub>4</sub>, there are some inherent issues with this approach.<sup>39,49,50</sup> First, the addition of an electrochemically inert binder and a conductivity enhancer lowers the overall gravimetric capacity of the cathode. As some formulations call for as high as 10% by/wt loading of the binder and carbon, a significant reduction in gravimetric capacity occurs. In addition, the loss in capacity makes it difficult to achieve high volumetric energy solutions. Finally, studies have shown that the carbon surrounding the active material can slow down the diffusion of the ions in and out of the active material.<sup>51</sup> In order to increase the stability and maintain the highest specific and gravimetric capacities, a new synthesis method for the fabrication of TiS<sub>2</sub> cathode insertion hosts that does not require the use of any binder or conductive additives is needed. Furthermore, scaling TiS<sub>2</sub> to nanoscale dimensions would offer the potential for increased power and energy densities due to an improved interfacial contact between TiS<sub>2</sub> and the electrolyte and shorter solid-state diffusion paths. Moreover, the fabrication of well-defined one-dimensional nanostructured TiS<sub>2</sub> arrays allows for better control of volume changes upon intercalation/de-intercalation without fracturing, –a phenomenon that is often observed in bulk or micron-sized materials.

In a previous publication, we reported the synthesis, electrical characterization, electrochemical properties, and the control of sulfur vacancies of TiS<sub>2</sub> cathode insertion hosts. As demonstrated in our earlier work, the systematic solid-state transformation of TiS<sub>3</sub> to TiS<sub>2</sub> nanobelts allows for the control of the nonstoichiometry in TiS<sub>2-x</sub> nanostructures.<sup>52</sup> Such control demonstrates that cathodes based on sulfur-deficient TiS<sub>2-x</sub> nanobelts deliver efficient Li<sup>+</sup> intercalation/de-intercalation activity, excellent cycling life, enhanced specific capacity, and excellent rate capability pointing to the importance of carefully controlling defects and stoichiometries in materials as a way to favorably tune their electronic properties. In this work, TiS<sub>3</sub> nanobelts are grown in a vertically oriented array directly on a metallic current collector substrate. Via a pyrolysis fabrication technique, the TiS<sub>3</sub> nanobelt array is further converted into a TiS<sub>2-x</sub> nanobelt array that can be used as a cathode without the addition of binders or carbon additives. The vertically oriented nanobelt array geometry allows for each TiS<sub>2-x</sub> nanobelt that is electrically connected to the metallic current collector substrate to contribute to the capacity. Moreover, each TiS<sub>2-x</sub> nanobelt has the ability to access various anisotropic 1D electronic pathways allowing for efficient

charge transport. We also report the effects that varied pyrolysis times have on the crystalline structure, induced S vacancies, and specific capacity of the vertically oriented  $\text{TiS}_{2-x}$  cathode insertion hosts. Similarly, we report the electrochemical properties of vertically oriented  $\text{TiS}_{2-x}$  nanobelt arrays, the effect of different charge and discharge rates on their capacity, and their long-term stability when incorporated into both Li-ion and Na-ion battery systems. Finally, we discuss the changes in diffusion rates for Li- and Na-ions upon their insertion into vertically oriented  $\text{TiS}_{2-x}$  nanobelt arrays via studies involving Galvanostatic intermittent titration techniques (GITT).

## Experimental methods

### Synthesis

Titanium (Ti) sputtering target (Kurt J. Lesker 99%, 1.0" Dia. X 0.125" thick) and sulfur (S) powder (Alfa Aesar 99.5%, ~100 mesh) were used as received without any purification or further treatment. All work was performed using Schlenk-line techniques or performed in an argon-filled glovebox to limit oxygen and water exposure. To synthesize  $\text{TiS}_3$  nanobelt arrays, a 1.6  $\mu\text{m}$ -thick Ti film was first sputtered onto a carbon-coated Al (C-Al) foil (MTI) using a Denton Discover 18 sputtering system. This process yielded a 5/8" x 3" piece of Ti-coated C-Al foil that was subsequently placed into a borosilicate ampule with  $\approx 85$  mg of S powder. The ampule was evacuated to  $\approx 10^{-3}$  torr using a vacuum line prior to flame-sealing. The sealed ampule was heated in a furnace to 450 °C at 10 °C/min and then isothermed at 450 °C for 20 h. The ampule was then removed from the oven and placed on an Al block to induce rapid quenching of the reaction. For the conversion of  $\text{TiS}_3$  nanobelts to  $\text{TiS}_{2-x}$  nanobelts, the as-prepared  $\text{TiS}_3$ -coated substrate was transferred to a new borosilicate ampule. A glass wool plug was added into the ampule as a constriction to prevent the precursors from coming into physical contact during handling. Subsequently,  $\approx 150$  mg of Ti powder (Alfa Aesar 99%, ~325 mesh) was added while being kept separated from the  $\text{TiS}_3$  precursor. This was performed to allow Ti to react with volatilized sulfur that has been pyrolyzed from the  $\text{TiS}_3$  sacrificial template. The ampule containing the  $\text{TiS}_3$  sacrificial template along with the Ti powder precursor was evacuated and flame-sealed under vacuum. The reaction ampule was placed in a furnace and heated to 450 °C at 10 °C/min and then isothermed at 450 °C for 48 – 144 h. The reaction ampule containing the  $\text{TiS}_{2-x}$  nanobelts was allowed to cool to ambient temperature inside of the furnace.

### Characterization

The morphologies of the resulting products were examined using a scanning electron microscope (SEM) equipped with a field-emission gun (FEI Nova Nano, FE-SEM 630) operated at an accelerating voltage of 10 keV. Phase

identification and purity of the as-synthesized  $\text{TiS}_3$  and  $\text{TiS}_{2-x}$  nanobelts were obtained by x-ray diffraction (XRD) using a Bruker D8 Advance diffractometer, at a scanning rate of  $1.2^\circ \text{min}^{-1}$  in a  $2\theta$  range between  $5^\circ$  and  $70^\circ$  using monochromated Cu K $\alpha$  radiation ( $\lambda = 1.5406 \text{ \AA}$ ). The operating voltage and current were kept at 40 kV and 40 mA, respectively. The dimensions and crystallinity of the as-synthesized nanobelts were examined using a JEOL JEM 2800 field-emission gun transmission electron microscope (FE-TEM) operated at 200 keV. High-resolution TEM (HRTEM) images and selected area electron diffraction (SAED) patterns were independently acquired and provided insights into the crystal growth habits and crystallinity of the  $\text{TiS}_3$  and  $\text{TiS}_{2-x}$  nanobelts, respectively. To prepare the samples for TEM/SAED analysis, the nanobelts were dispersed in 2-propanol via sonication and then deposited onto a 400-mesh holey carbon-coated copper grid. For spectroscopy measurements, all films fabricated were handled in an inert Ar atmosphere and never exposed to oxygen and water levels above 1 ppm before introduction into the ultra-high vacuum (UHV) system for x-ray photoelectron (XPS) and ultraviolet photoelectron (UPS) spectroscopy measurements. XPS and UPS spectra were acquired in a custom-built UHV chamber equipped with a cylindrical mirror electron analyzer and operated at a base pressure of  $10^{-10}$  Torr. UPS was performed by using a He I (21.22 eV) excitation line of a He plasma in a discharge lamp. Spectra were taken at a pass energy of 5 eV for a nominal experimental resolution smaller than 150 meV. XPS was performed on an additional sample series, using the Al K $\alpha$  line (1487.6 eV) with a resolution of 0.8 eV. A pass energy of 100 eV was used for survey scans, while a 40 eV pass energy was used for detailed scans. All measurements were carried out at normal take-off angles. The acquired spectra were calibrated against an adventitious carbon peak at 284.6 eV. Curve fitting was carried out using CasaXPS software with a Gaussian-Lorentzian product function and a non-linear Shirley background.

### Electrochemical studies

Cathodes were fabricated by punching  $\frac{1}{2}$ " diameter discs from the  $\text{TiS}_{2-x}$ -coated C-Al foil substrate. Each disc had approximately 1.5 – 1.7 mg of  $\text{TiS}_{2-x}$  nanobelts. CR2032 coin cells were assembled in an Ar-filled glovebox using the cathode prepared above and Li(Na) foil as the anode. Celgard (2400) was used as the separator. A 1.0 M  $\text{LiPF}_6$  (for Li-ion battery) and 1.0 M  $\text{NaPF}_6$  (for Na-ion battery) in ethylene carbonate/diethyl carbonate (50/50 v/v) solutions were used as the electrolytes. The batteries were constructed in the following manner: bottom cup, cathode, electrolyte (25  $\mu\text{l}$  for Li-ion and 30  $\mu\text{l}$  for Na-ion), separator, electrolyte (25  $\mu\text{l}$  for Li-ion and 30  $\mu\text{l}$  for Na-ion), anode, Ni foam, and the top cap.

Galvanostatic measurements were conducted at room temperature using a Neware BT-4008 battery testing system. Li-ion cells were cycled between 1.0 V and 3.0 V

versus  $\text{Li}^+/\text{Li}$ . Na-ion cells were cycled between 0.5 V and 2.5 V versus  $\text{Na}^+/\text{Na}$ . The capacity retention study was cycled at different rates ranging from 0.2 – 5 C. The long-term capacity fade study was cycled at a theoretical rate of 0.1 C. The specific capacity and coulombic efficiency calculations are determined within a  $\pm 1\%$  uncertainty error. The GITT study was discharged at a theoretical rate of 0.2 C. All batteries tested for the GITT study were discharged for 1 minute and then allowed to rest for 2 hours before the next discharge.

Electrochemical impedance spectroscopy (EIS) and cyclic voltammetry (CV) studies were performed on a CH Instrument (CHI660E) electrochemical workstation. Each test was performed using a CR2032 coin cell. Frequency ranges from 100 MHz to 0.1 Hz and an amplitude of 10 mV were used. EIS spectra were fit to the equivalent electrical circuit presented in **Figure 7** using a CHI Version 14.09 software.

## Results and Discussion

Both  $\text{TiS}_3$  and  $\text{TiS}_2$  exhibit a lamellar structure that makes them ideal intercalation host materials.  $\text{TiS}_3$  has a monoclinic crystal structure that consists of infinite 2D double layers of  $\text{TiS}_3$  polyhedra. Each polyhedron is comprised of two  $\text{S}_2^{2-}$  ions in a rectangular face and four noncoplanar  $\text{S}^{2-}$  ions. The double layers are formed by sharing the  $\text{S}^{2-} - \text{S}^{2-}$  edges between the 1D single layers.

particularly 2D metal chalcogenides– to nanoscale dimensions may provide an incredible bounty of advantages such as improved accommodation of strain defects upon electrochemical lithiation/sodiation, increased electrode/electrolyte interaction, and shorter diffusion path lengths.<sup>55, 56</sup>  $\text{TiS}_3$  tends to crystallize as anisotropic structures due to its crystal structure having two easy cleavage planes both of which ease the reduction of bulk  $\text{TiS}_3$  into belt-like nanostructures.  $\text{TiS}_2$ , in contrast, tend to crystallize as isotropic structures that often yield very irregular and undefined plate-like structures. Since these plate-like structures tend to be very inhomogeneous and poorly size controllable, it is extremely challenging to accurately determine how quantum confinement, morphology, and orientation affect the electrochemical properties of  $\text{TiS}_2$ . Here, we developed a fabrication method for the synthesis of well-defined and vertically oriented  $\text{TiS}_3$  nanobelt arrays. These  $\text{TiS}_3$  nanobelt arrays form the sacrificial scaffolding that is then pyrolyzed to yield  $\text{TiS}_{2-x}$  while preserving the nanobelt morphology and vertically aligned array orientation. The pyrolysis conversion (desulfurization) of  $\text{TiS}_3$  nanobelts into  $\text{TiS}_{2-x}$  nanobelts proceeds according to the following chemical reaction:

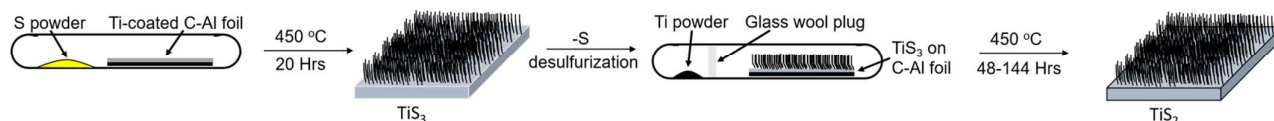
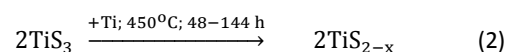
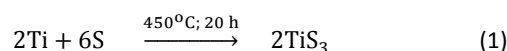


**Figure 1.** Schematic depiction for the synthesis of vertically oriented  $\text{TiS}_3$  nanobelt arrays and their subsequent conversion into vertically oriented  $\text{TiS}_{2-x}$  nanobelt arrays.

Conversely, the space between the  $(\text{S}_2^{2-})_2$  ion rectangular faces is empty, thus providing the necessary room for the intercalation and deintercalation of  $\text{Li}^+$  and  $\text{Na}^+$  ions.<sup>53</sup>  $\text{TiS}_3$  has a higher theoretical specific capacity ( $556\text{ mAh g}^{-1}$ ) than that of  $\text{TiS}_2$  ( $239\text{ mAh g}^{-1}$ ). However, when  $\text{TiS}_3$  is incorporated into liquid-type Li-ion cells, its experimental specific capacity quickly fades from  $\approx 350\text{ mAh g}^{-1}$  to  $\approx 75\text{ mAh g}^{-1}$  after the 5<sup>th</sup> cycle.<sup>54</sup> This abrupt capacity fading is caused by the structural degradation of  $\text{TiS}_3$  upon the irreversible reduction of  $\text{S}_2^{2-}$  to  $\text{S}^{2-}$  in the presence of organic liquid electrolytes.<sup>54</sup>  $\text{TiS}_2$  is comprised only of  $\text{S}^{2-}$  ions in its crystal structure and does not suffer from any structural degradation upon cycling. For these particular reasons,  $\text{TiS}_2$  has been widely studied over  $\text{TiS}_3$  as a cathode insertion host despite having a lower theoretical specific capacity. Furthermore, given the remarkable enhancements of charge capacities and life cycles observed for anodes and cathodes comprising materials that are susceptible to finite size effects, it is now widely accepted that scaling materials –

During the desulfurization of  $\text{TiS}_3$ , nucleation seeds comprising  $\text{TiS}_2$  facets are formed on the surface of the  $\text{TiS}_3$  nanobelts and are propagated inward at a rate that is strongly dependent on the reaction time and temperature. As depicted in **Figure 1**,  $\text{TiS}_3$  is initially formed by the interaction of sulfur (vapor-phase) with elemental titanium (solid-phase) atop a C-Al foil substrate. This interaction yields a vertically oriented  $\text{TiS}_3$  nanobelt array. Crucial to the fabrication of vertically oriented  $\text{TiS}_{2-x}$  nanobelt arrays is the control of two competing reaction dynamics, i.e., the high-temperature removal of S from  $\text{TiS}_3$  and the possible disruption of the nanostructure morphologies due to these high temperatures. When heated, sulfur leaches out from the  $\text{TiS}_3$  sacrificial template. Here, a titanium source is introduced to avoid the re-absorption of sulfur by the  $\text{TiS}_3$  sacrificial template. A reaction temperature of  $450\text{ }^\circ\text{C}$  enables the conversion of  $\text{TiS}_3$  to  $\text{TiS}_{2-x}$  while preserving both the 1D morphology and vertically aligned orientation.<sup>52</sup>

The SEM micrographs presented in **Figure 2** illustrate the morphological features of the bare substrates and those of the vertically aligned nanostructures. **Figure 2A** shows the SEM image for a bare C–Al foil substrate. This C–Al foil substrate is highly porous with multiple voids being interconnected by a C–C network. Previous reports have demonstrated that cathodes made using C–Al foils as substrates exhibit higher initial capacity as well as less degradation over the cycling lifetime. This performance boost is attributed to greater adhesion strength of the current collector foils when carbon is present as compared to pristine current collector foils.<sup>57,58</sup> As shown in **Figure 2B**, upon sputtering Ti onto the C–Al foil, the voids are filled in with a thin layer of the metal, resulting in a pinhole free and non-porous surface. **Figure 2C** depicts the SEM image for an as-synthesized  $\text{TiS}_3$  vertically oriented nanobelt array. These nanobelt arrays are  $\approx 75 \pm 10 \mu\text{m}$  thick (based on statistical length distributions obtained from cross-sectional SEM images, **Figure S1**). The growth of the nanobelts is thought to proceed via a vapor–solid process involving the reaction between sulfur (in the vapor phase) and titanium (in the solid phase). Individual nanobelts obtained by the vapor transport reaction are  $\approx 65 \pm 10 \text{ nm}$  in width (based on statistical distributions obtained for 500 nanobelts) and  $\approx 85 \pm 3 \text{ nm}$  thick (from tapping mode atomic force microscopy measurements). Both dimensions are smaller than the average length of the nanobelt ( $\approx 75 \pm 10 \mu\text{m}$ ). **Figure 2D** shows the SEM image for a dense vertically aligned  $\text{TiS}_{2-x}$  nanobelt arrays showing the smooth walls and uniform morphology and sizes along the length of the nanobelts. The resulting nanobelts obtained from the desulfurization of the  $\text{TiS}_3$  sacrificial template are  $\approx 60 \pm 10 \text{ nm}$  in width and  $\approx 90 \pm 5 \text{ nm}$  thick suggesting that the pyrolysis process has little to no impact on the morphology and sizes of the final product, i.e., the  $\text{TiS}_{2-x}$  nanobelt arrays.

Definitive phase identification of the structures is obtained from XRD measurements. **Figure 3** depicts the XRD patterns of the vertically oriented  $\text{TiS}_3$  nanobelt array substrate upon annealing at  $450 \text{ }^\circ\text{C}$  and being exposed to different desulfurization reaction times (48 – 144 h). As a control, the XRD spectrum for a bare C–Al foil is also presented. Besides from the peaks ascribed to the C–Al substrate (denoted with a “C”), all experimental reflection peaks can be assigned either to  $\text{TiS}_3$  (Joint Committee of Powder Diffraction Standards (JCPDS) No. 15–0783) or  $\text{TiS}_2$  (JCPDS No. 15–0853). As illustrated in **Figure 3**, the initial contact between sulfur and titanium only yields  $\text{TiS}_3$  as the main product. When pyrolyzed for 48 h,  $\text{TiS}_3$  is fully converted to a phase that is closer to that of stoichiometric  $\text{TiS}_2$ . As previously determined, fabricating stoichiometric  $\text{TiS}_2$  may be challenging due to its tendency to develop sulfur vacancies and/or titanium adatoms.<sup>52</sup> Since it is challenging to control the stoichiometry of  $\text{TiS}_2$ , it is also troublesome to accurately determine its electrical and physicochemical

properties as these are mostly interrelated to the amount of vacancies and defects introduced during the fabrication process. For this purpose, we will refer to the as-pyrolyzed products as  $\text{TiS}_{2-x}$ , where the prolonged desulfurization exposure produces a Ti/S stoichiometry ratio that is farther away from the nominal  $\text{TiS}_2$  stoichiometry.

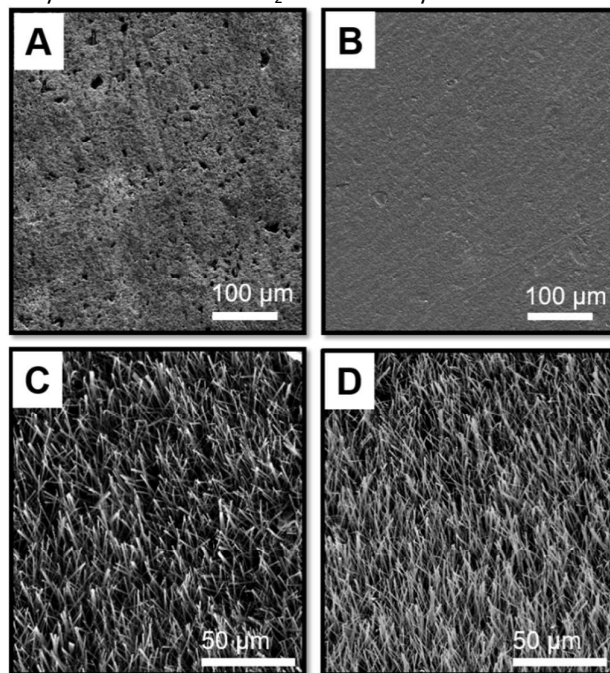


**Figure 2.** SEM images for a pristine C–Al foil substrate (A), Ti-coated C–Al foil substrate (B), as-synthesized  $\text{TiS}_3$  (C) and  $\text{TiS}_{2-x}$  vertically oriented nanobelt arrays (D).

Further structural and morphological studies on individual  $\text{TiS}_3$  and  $\text{TiS}_{2-x}$  nanobelts have been undertaken using lattice-resolved HRTEM and SAED (**Figure 4**). The patterns obtained from both HRTEM and SAED allow for the elucidation of the single-crystalline nature of the  $\text{TiS}_3$  sacrificial template and its pyrolysis to yield  $\text{TiS}_{2-x}$  nanobelt arrays. The lattice-resolved HRTEM image shown in **Figure 4A** shows three distinct lattice fringes with interplanar spacings of 2.01, 2.28, and 4.93 Å. The observed spacing between the lattice fringes can be assigned to the (210), (112) and (100) crystallographic planes of the  $\text{TiS}_3$  crystal structure, respectively. **Figure 4B** shows the SAED pattern for an individual  $\text{TiS}_3$  nanobelt. This pattern is consistent along the length of the nanobelt corroborating its single-crystalline nature. The diffraction spots observed in the SAED pattern presented in **Figure 4B** are associated with the crystallographic reflection planes from the  $\text{TiS}_3$  monoclinic crystal structure. The full conversion of  $\text{TiS}_3$  to  $\text{TiS}_{2-x}$  nanobelt arrays also results in the formation of a single-crystalline product as corroborated in the lattice-resolved HRTEM and SAED patterns presented in **Figure 4C,D**. The lattice-fringes observed in the HRTEM micrograph presented in **Figure 4C** are spaced at 1.70 and 2.95 Å, which corresponds to the lattice spacing between the (110) and

(100) planes of the  $\text{TiS}_2$  crystal structure, respectively. The SAED pattern presented in **Figure 4D** exhibits a six-fold symmetry ( $\sim 60^\circ$  oriented with respect to the (010) and (100) planes) that is characteristic of  $\text{TiS}_2$  having a hexagonal crystal structure. Based on both HRTEM and SAED analyses,  $\text{TiS}_3$  and  $\text{TiS}_{2-x}$  nanobelts have a preferred growth direction along their  $c$ -axis. This preferred growth direction can readily facilitate the cleavage of  $\text{TiS}_3$  and  $\text{TiS}_{2-x}$  layered structures into few atoms-thick layers thus potentially unraveling unconventional properties due to quantum confinement effects.

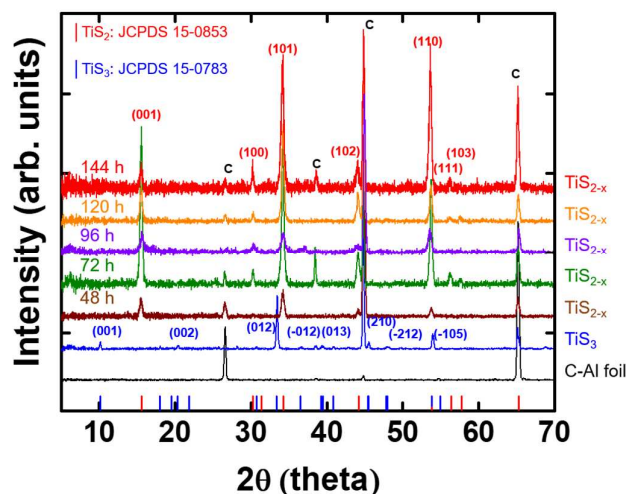


**Figure 3.** XRD spectra for a C-Al substrate,  $\text{TiS}_3$ , and  $\text{TiS}_{2-x}$  as a function of pyrolysis (desulfurization) reaction time. Peaks from the C-Al foil substrate are denoted with the letter “C”. The JCPDS for  $\text{TiS}_3$  and  $\text{TiS}_2$  crystal structures are presented as solid vertical lines at the bottom of the XRD patterns.

To further confirm the composition, purity, and coordination environment of the samples fully converted from  $\text{TiS}_3$  to the  $\text{TiS}_{2-x}$  nanobelt arrays, high-resolution XPS analyses for sulfur and titanium binding energy regions were performed. **Figure 5A** exhibits the XPS spectrum acquired for the Ti 2p region of the  $\text{TiS}_3$  sacrificial template. Here, the XPS spectrum features two distinct peaks centered at  $\approx 456.3$  and  $462.4$  eV. These two peaks are ascribed to Ti  $2p_{3/2}$  and Ti  $2p_{1/2}$ , respectively, with a spin-orbit doublet splitting of 6.1 eV. Such spin-orbit doublet splitting is characteristic of an oxidation state of 4+ for the Ti atoms present in  $\text{TiS}_3$ .<sup>54, 59</sup> **Figure 5B** depicts a slightly more convoluted XPS spectrum of the S 2p region for the as-prepared  $\text{TiS}_3$  nanobelts. The S 2p XPS spectrum is composed of three peaks at  $\approx 161.2$ ,  $162.4$  and  $163.6$  eV.  $\text{TiS}_3$  is notorious for having two different sulfur species, i.e.  $\text{S}^{2-}$  and  $\text{S}_2^{2-}$  which can be clearly identified by XPS. By analyzing the XPS spectrum presented in **Figure 5B**, we observe that the peak centered at  $\approx 161.2$  eV can be assigned to the  $\text{S}^{2-} 2p_{3/2}$  binding mode. The peak centered at  $\approx 162.4$  eV is a combination of the  $\text{S}^{2-} 2p_{1/2}$  and the  $\text{S}_2^{2-} 2p_{3/2}$  binding modes. Finally, the peak centered at  $\approx 163.6$  eV can

be assigned to the  $\text{S}_2^{2-} 2p_{1/2}$  binding mode. The fit ratio of the  $\text{S}_2^{2-}:\text{S}^{2-}$  peak areas is 2:1, indicating that  $\text{TiS}_3$  is comprised of one  $\text{S}_2^{2-}$  and one  $\text{S}^{2-}$  units.<sup>54, 59</sup> **Figure 5C** shows the Ti 2p XPS spectrum obtained for a pyrolyzed  $\text{TiS}_3$  substrate upon full conversion to  $\text{TiS}_{2-x}$  (reaction temperature:  $450^\circ\text{C}$ ; pyrolysis time exposure: 48 h). Here, we observe the evolution of the Ti  $2p_{3/2}$  and Ti  $2p_{1/2}$  doublet peaks centered at  $\approx 456.3$  and  $462.4$  eV, respectively. These peaks, are again, characteristics of  $\text{Ti}^{4+}$ . **Figure 5D** shows the XPS spectrum of the S 2p region for the fully converted  $\text{TiS}_{2-x}$  sample. The S 2p peaks are a slightly merged doublet that is fit to S  $2p_{3/2}$  and S  $2p_{1/2}$  centered at 161.2 and 162.4, respectively, with a spin-orbit doublet splitting of 1.2 eV. As depicted in **Figure 5D**, the lack of any peaks associated with  $\text{S}_2^{2-}$  further corroborates the full conversion of  $\text{TiS}_3$  to  $\text{TiS}_{2-x}$ . It is worth mentioning, that the XPS spectra presented in **Figure 5C,D** are representative of all samples obtained by the pyrolysis of  $\text{TiS}_3$  for 48 – 144 h. We do not observe the evolution of any peaks that could potentially be associated with the decomposition of  $\text{TiS}_{2-x}$  into sub-stoichiometric Ti/S structures upon prolonged desulfurization.

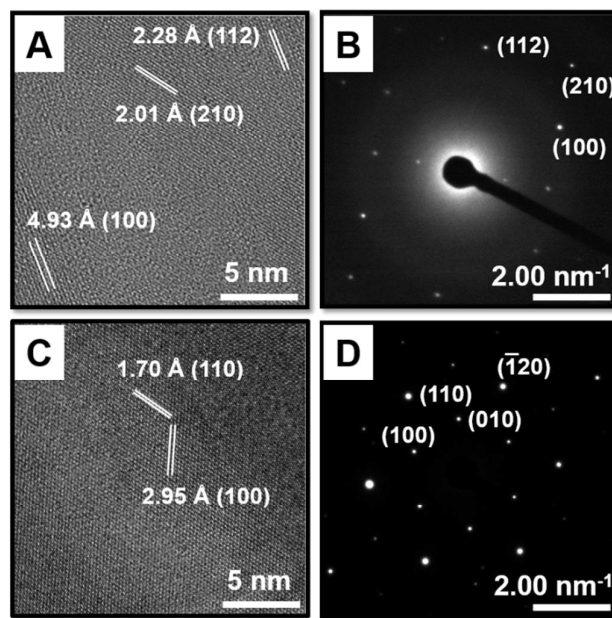


**Figure 4.** HRTEM images for  $\text{TiS}_3$  and  $\text{TiS}_{2-x}$  single nanobelts. (A) Lattice-resolved HRTEM image for an individual  $\text{TiS}_3$  nanobelt. (B) Indexed SAED pattern for  $\text{TiS}_3$ . (C) Lattice-resolved HRTEM image for an individual  $\text{TiS}_{2-x}$  nanobelt. (D) Indexed SAED pattern for  $\text{TiS}_{2-x}$ . The sample used for acquiring the HRTEM data in C and D was pyrolyzed at  $450^\circ\text{C}$  for 48 h.

As discussed above, a problem that has deterred  $\text{TiS}_2$  from being considered a viable material for energy storage – despite its superb electrochemical properties – is the inability to synthesize well-controlled stoichiometric  $\text{TiS}_2$  structures. In the early 1960s, work by Bernard and Jeannin argued that

Ti atoms would occupy interstitial sites and therefore the  $\text{TiS}_2$  structure would be metal-rich.<sup>60</sup> They claimed that the metallic nature of  $\text{TiS}_2$  arises from degenerate states created by excess Ti atoms in the crystal structure. Further investigations done by Thompson *et al.*, proved that stoichiometric  $\text{TiS}_2$  does exist and that the metallic behavior must arise from some other source.<sup>61</sup> Another plausible explanation is that instead of being metal rich due to Ti atoms occupying interstitial sites, it may be that  $\text{TiS}_2$  is sulfur deficient thus, creating S vacancies. If a sulfur vacancy occurs, the electron participating in the bonding is transferred to the  $\text{Ti}^{4+}$  atom thus reducing it to  $\text{Ti}^{3+}$ . One way to probe the electronic and defect states of  $\text{TiS}_{2-x}$  is via ultraviolet photoelectron spectroscopy (UPS) studies.

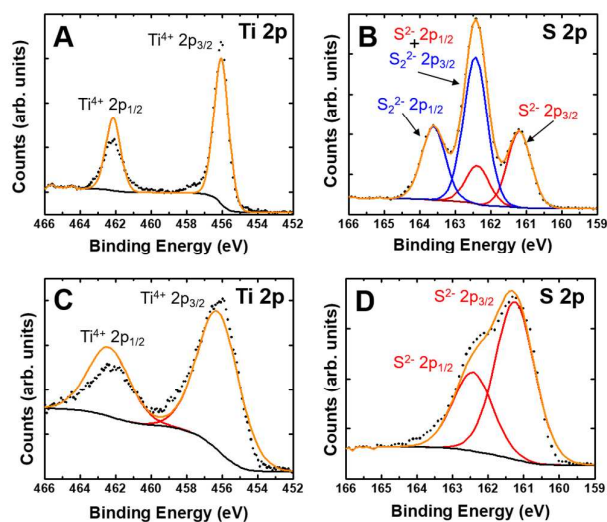


**Figure 5.** XPS spectra for vertically oriented  $\text{TiS}_3$  and  $\text{TiS}_{2-x}$  nanobelt arrays. (A,B) Ti 2p and S 2p regions, respectively, for  $\text{TiS}_3$ . (C,D) Ti 2p and S 2p regions, respectively, for  $\text{TiS}_{2-x}$ . The sample used for acquiring the XPS data in C and D was pyrolyzed at 450 °C for 48 h.

Using ultraviolet radiation, the occupied states at the top of the valence band and below the Fermi level are probed. **Figure 6** shows the direct photoemission spectra –around the valence band onset– of  $\text{TiS}_{2-x}$  with different sulfur vacancy concentrations. The Fermi level is referenced to a binding energy of 0 eV. Besides the normal secondary electron energy cutoff observed at a binding energy of  $\approx 1$  eV below the Fermi level, there is the evolution of a peak at a binding energy of  $\approx 0.3$  eV around the Fermi edge. This feature is attributed to  $\text{Ti}^{3+}$  3d band defect states that arise when S vacancies are present. To determine how the  $\text{Ti}^{3+}$  3d band defect states changes during the desulfurization process, the signals were normalized using the secondary energy cutoff as the base. The inset provided in **Figure 6** shows the growth of the  $\text{Ti}^{3+}$  3d band defect state feature as the pyrolysis time is increased. This suggests that upon prolonged desulfurization time exposure of  $\text{TiS}_3$  in order to

convert it to  $\text{TiS}_{2-x}$ , the likelihood for the formation of sulfur-deficient nonstoichiometric  $\text{TiS}_2$  structures is increased. This tendency of developing anion vacancies in titanium compounds has been previously demonstrated for oxygen-deficient  $\text{TiO}_x$  structures via similar UPS studies.<sup>62,63</sup>

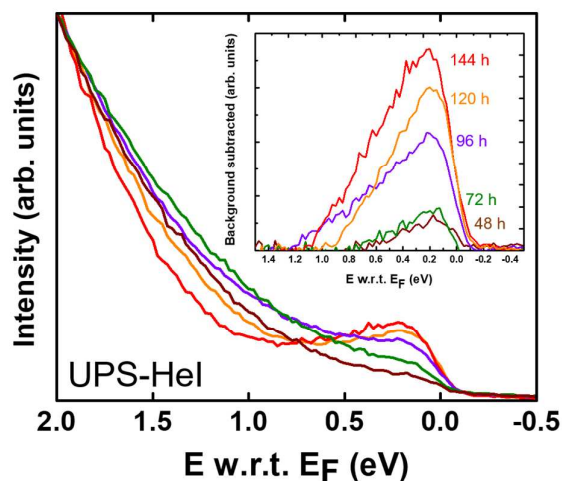


**Figure 6.** UPS spectra near the Fermi level for vertically oriented  $\text{TiS}_3$  and  $\text{TiS}_{2-x}$  nanobelt arrays. Shoulder features near the Fermi level indicate the presence of  $\text{Ti}^{3+}$  band defect states. Inset shows background subtracted peaks illustrating the ingrowth of the  $\text{Ti}^{3+}$  3d band defect peak upon prolonged desulfurization time exposure.

While the electrochemical performance of an energy storage device may be improved through the incorporation of novel materials with unconventional properties, designing conformal energy storage devices comprising 1D nanoarrays in a 3D architecture may fundamentally provide superior advantages (*vide infra*). As a model architecture in high power Li (Na)-ion batteries, self-supported 1D nanoarrays that can serve as vertically oriented electrodes enable high power densities as a result of their increased surface area. Theoretically,  $\text{Li}^+$  ( $\text{Na}^+$ ) diffusion time is directly proportional to the square of the diffusion length. Thus, reducing the  $\text{Li}^+$  ( $\text{Na}^+$ ) diffusion pathway decreases the diffusion time scales. Specifically, fabricating an electrode in a vertically oriented architecture where the ion diffusion path is perpendicular to the current collector holds tantalizing possibilities for enhanced ion delivery while maintaining fast electron transport. Here, we fabricated binder- and carbon-free vertically oriented  $\text{TiS}_{2-x}$  nanoarray electrodes directly grown on the current collector. **Figure 7** shows the electrochemical performance for our vertically oriented  $\text{TiS}_{2-x}$  nanobelt arrays as cathode insertion hosts in a half-cell configuration (Li/Na- $\text{TiS}_{2-x}$ ). Upon cycling both Li- and Na-based  $\text{TiS}_{2-x}$  half-cells, no significant changes in the cyclic voltammetry (CV) characteristics are observed (**Figure S2**). This suggests that  $\text{TiS}_{2-x}$  nanobelt arrays do not undergo any phase transformations upon cycling or during the formation of the SEI layer. This result is in accordance with a previous report

demonstrating the effective intercalation of  $\text{Li}^+$  ions within the layers of  $\text{TiS}_2$  nanobelts without any significant structural disruption.<sup>64</sup>

The CV curves for the Li-based half-cell within the potential region of 1 – 3 V (vs.  $\text{Li}/\text{Li}^+$ ) at a scan rate of 5 mV/s is shown in **Figure 7A**. The discharge profile for the Li-based  $\text{TiS}_{2-x}$  half-cell exhibits two peaks centered at  $\approx 1.8$  and 1.6 V. Within this voltage window, the  $\text{Ti}^{4+}/\text{Ti}^{3+}$  is the only observable redox couple. The two peaks upon lithium intercalation are attributed to lithium rearrangement within the  $\text{TiS}_{2-x}$  host matrix as the lithium loading approaches one Li per  $\text{TiS}_2$  unit. This behavior is often observed in high-voltage oxide-based intercalation cathodes. The de-intercalation of lithium within the  $\text{TiS}_{2-x}$  host matrix occurs at 2.3 V. Taking into consideration the redox waves for the lithium intercalation and de-intercalation process taking place at 1.7 (median value) and 2.3 V, respectively, a charge-discharge overpotential of  $\approx 0.6$  V is observed. Conversely, as shown in **Figure 7B**, the CV curves for the Na-based  $\text{TiS}_{2-x}$  half-cell within the potential region of 0.5 – 2.5 V (vs.  $\text{Na}/\text{Na}^+$ ) at a scan rate of 5 mV/s display a single peak at 1.1 V for the intercalation of Na into the  $\text{TiS}_{2-x}$  matrix followed by a de-intercalation peak at 1.9 V. A charge/discharge overpotential of  $\approx 0.8$  V is observed for the Na-based  $\text{TiS}_{2-x}$  system. Due to Na having a larger ionic radius than that of Li, Na intercalation/de-intercalation would require a higher driving force to occur. Previous demonstrations using  $\text{LiNi}_{1/3}\text{Co}_{1/3}\text{Mn}_{1/3}\text{O}_2$  as an active cathode material have shown that an increased overpotential results in a decrease in specific capacity.<sup>65</sup> As such, when fabricating batteries and understanding the electrochemical performance of our vertically oriented  $\text{TiS}_2$  nanobelt arrays as cathode insertion hosts, it would not be surprising that Na-based  $\text{TiS}_2$  devices will show lower discharge specific capacities than that of Li-based  $\text{TiS}_2$  devices (*vide infra*).

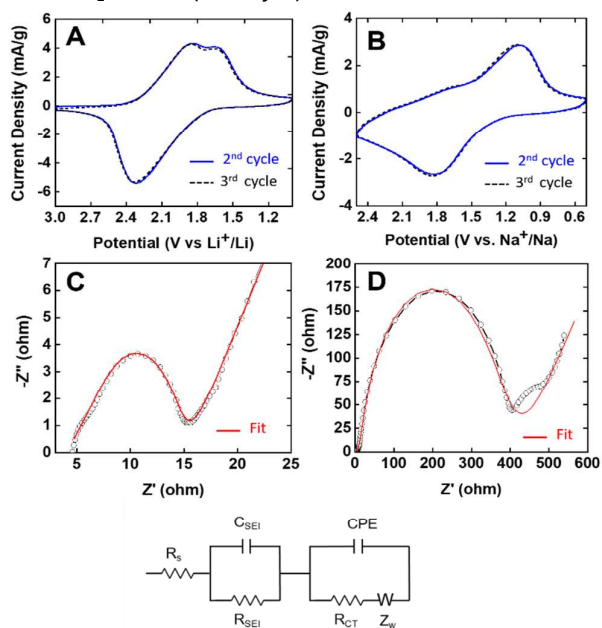
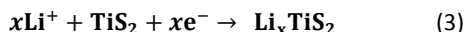


**Figure 7.** Cyclic voltammetry characteristics of the second and third cycles for a vertically oriented  $\text{TiS}_{2-x}$  nanobelt array cathode in an assembled CR3032 cell with Li (A) and Na (B) as the anodes. Electrochemical impedance spectra for the Li- and Na- $\text{TiS}_2$  half cells shown in (C) and (D), respectively. The simulated Randle's equivalent circuit used for fitting the experimental data is also included in the figure. In this circuit,  $R_s$  is equivalent series resistance,  $R_{CT}$  is the charge-transfer resistance,  $R_{SEI}$  is the resistance of the electrode-electrolyte interphase,  $Z_w$  is the Warburg impedance element,  $C_{SEI}$  and CPE are the SEI and double layer capacitances, respectively. Each cathode was pyrolyzed at 450 °C for 48 h.

Electrochemical impedance spectroscopy (EIS) measurements yield insights into the charge transport, resistances, and interfacial processes in our Li (Na)-based  $\text{TiS}_{2-x}$  electrochemical systems. **Figure 7C, D** show the EIS data in the form of Nyquist plots for Li- $\text{TiS}_{2-x}$  and Na- $\text{TiS}_{2-x}$  half-cells. The EIS measurements were acquired at the open circuit potential for each cell after the 50<sup>th</sup> charge-discharge cycle. For both type of cells, we observe the formation of a quasi-semicircle at high frequencies. The low frequency region, however, is comprised of a quasi-linear tail. The front edge of the semi-circle is a function of the resistance and capacitance of the formed solid-electrolyte interface. The later part of the semi-circle is derived from the charge-transfer resistance and it is associated to the double-layer capacitance. The quasi-linear tail observed at low frequencies is a product of the Warburg impedance element associated with ion diffusion. When fit to the equivalent circuit also presented in **Figure 7**, the EIS data allow for the determination of the resistances within the Li(Na)-based  $\text{TiS}_{2-x}$  half-cells. Based on the equivalent circuit,  $R_s$  represents the ohmic series resistance of the electrolyte (resistances from the current collectors, separators, and electrodes may play a minor role in the magnitude of the ohmic resistance),  $R_{SEI}$  denotes the resistance of the solid-electrolyte interphase (SEI) formed on the electrode surfaces,  $C_{SEI}$  is the capacitance of the SEI layer,  $R_{CT}$  is the resistance developed upon charge transfer,  $C_{CT}$  is the double layer capacitance, and  $W$  corresponds to the Warburg impedance due to the diffusion of  $\text{Li}^+$  ( $\text{Na}^+$ ) ions into the electrode. By fitting the EIS data, we obtain a low  $R_s$  of  $\approx 4.2$   $\Omega$ , which is indicative of the good electrochemical cycling stability of our vertically oriented  $\text{TiS}_{2-x}$  nanobelt arrays as cathode insertion hosts for Li-ion batteries. Also, a low  $R_{CT}$  of  $\approx 6.9$   $\Omega$  is obtained which suggests a fast rate of redox reactions at the electrode-electrolyte interface and it is also indicative of fast Li-ion transport within the vertically oriented  $\text{TiS}_{2-x}$  scaffold. In addition, a low  $R_{CT}$  could also be associated with an increased contact area at the electrode-electrolyte interface upon introducing the vertically oriented nanobelt arrays. The  $R_{SEI}$  which is the leakage resistance at the SEI layer is usually very high and can be ignored in the circuit. In contrast, as shown in **Figure 7D**, a larger semi-

circle radius is obtained for the Na-based  $\text{TiS}_{2-x}$  half cells. The fit data yields a  $R_s$  and  $R_{CT}$  of  $\approx 5.0$  and  $151.4 \Omega$ , respectively. The resistance values calculated for Na-based  $\text{TiS}_{2-x}$  are higher than those obtained for Li-based  $\text{TiS}_{2-x}$  indicating that there is a larger electron transfer resistance for Na-ion transport between the vertically oriented  $\text{TiS}_{2-x}$  matrix host and the electrolyte.

Since the fabrication of our vertically oriented  $\text{TiS}_{2-x}$  arrays provide a well-defined percolating network comprising highly conducting nanobelts, it is now possible to utilize them as carbon- and binder-free cathode insertion hosts for Li- and Na-ion energy storage devices. The electrochemical performance of our vertically oriented  $\text{TiS}_{2-x}$  nanobelt arrays was evaluated using CR2032 coin cells in a half-cell configuration using either Li or Na as counter/reference electrodes. The galvanostatic charge-discharge performances of our vertically oriented  $\text{TiS}_{2-x}$  nanobelt arrays, when used as electrodes in Li(Na)-ion batteries are presented in **Figure 8**. The cycling stability and rate capabilities at different current densities and as a function of desulfurization time are studied in depth. The vertically oriented  $\text{TiS}_{2-x}$  nanobelt arrays used as cathodes were pyrolyzed for 48 – 144 h. Each cell was galvanostatically charged/discharged at a current density between 0.2 – 5 C, for ten cycles at each current density. **Figure 8A** shows the specific discharge capacities at various current densities for Li-based  $\text{TiS}_{2-x}$  half-cells. At a current density of 0.2 C, a discharge capacity of  $\approx 216 \text{ mAh g}^{-1}$  is obtained for a cathode that is pyrolyzed for 48 h. At the same current density (0.2 C), there is almost a 50% loss in capacity ( $\approx 110 \text{ mAh g}^{-1}$ ) when the  $\text{TiS}_{2-x}$  cathodes are further pyrolyzed for 144 h. To explain the drop-off in capacity, we will have to refer to the following reaction using the lithiation process as a model:



According to reaction 3, the Ti atom is reduced from a 4+ state to a 3+ state upon  $\text{Li}^+$  insertion. If there are S vacancies present and the Ti atom already exists in the 3+ oxidation state, that Ti atom can no longer contribute to the electrochemical capacity of the electrode. This would imply that the greater the number of S vacancies, the lower the overall discharge of the  $\text{TiS}_{2-x}$  cathode. Additionally, as the current density rate is increased from 0.2 to 5 C, a typically observed drop-off in specific capacity is also observed (regardless of the desulfurization exposure time). However, when the half-cells are again charged/discharged at a rate of 0.2 C, we observe the recovery of the specific capacity closer to that of the theoretical capacity ( $239 \text{ mAh g}^{-1}$ ). This capacity recovery suggests that the rapid intercalation/de-intercalation at higher current densities does not irreversibly affect the crystal structure and layered nature of the  $\text{TiS}_{2-x}$  nanobelts. Furthermore, as previously discussed, the specific capacity for Li-based half-cell comprising our vertically

oriented  $\text{TiS}_{2-x}$  nanobelt arrays pyrolyzed for 48 h is  $216 \text{ mAh g}^{-1}$ . Using the theoretical specific capacity for  $\text{TiS}_2$  of  $239 \text{ mAh g}^{-1}$ , the loading of Li would be  $\text{Li}_{0.90}\text{TiS}_{2-x}$ . **Figure 8B** shows a similar trend for the Na-based  $\text{TiS}_{2-x}$  half-cells. The Na-ion intercalation proceeds similarly to that of what is observed for Li-ion intercalation (reaction 2). However, due to the increased size of the Na-ion, it is argued that there is a limit on the amount of Na that can be incorporated into  $\text{TiS}_2$ . This limit has been previously determined to be 0.8 Na equivalent atoms per  $\text{TiS}_2$  formula thus it is expected that the specific discharge capacity for Na-based  $\text{TiS}_2$  would be lower than that obtained for Li-based  $\text{TiS}_2$  half-cells.<sup>46, 47</sup> As depicted in **Figure 8B**, at a 0.2 C rate, the specific capacity for Na-based  $\text{TiS}_{2-x}$  pyrolyzed for 48 h is  $190 \text{ mAh g}^{-1}$ . Using the theoretical specific capacity, the loading of Na would be  $\text{Na}_{0.80}\text{TiS}_{2-x}$ . Ignoring any capacity losses due to sulfur vacancies, which are relatively low for the cathodes pyrolyzed for 48 h, the Na loading is in agreement with previously reported values.<sup>46, 47</sup> In terms of morphology and possible structural changes that our  $\text{TiS}_{2-x}$  electrodes may undergo upon cycling, we observe that after closing the coin cell, the very top layer of the nanobelt array is completely pressed against the cap. However, the overall nanobelt morphology and structure are preserved before and after electrochemical cycling (**Figure S3**).

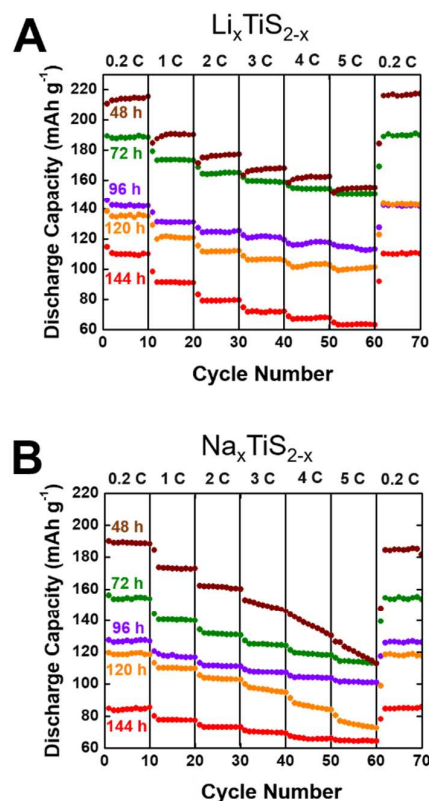


**Figure 8.** Specific discharge capacities at various current densities for vertically oriented  $\text{TiS}_{2-x}$  nanobelt arrays used as cathode insertion hosts in Li (A) and Na (B) half-coin cells.

Cathodes were pyrolyzed at 450 °C for several time intervals ranging from 48 – 144 h.

The long-term cycling stability of the vertically oriented  $\text{TiS}_2$  cathode was studied by cycling the Li- and Na- based  $\text{TiS}_{2-x}$  half-cells at a rate of 0.1 C for 100 cycles. **Figure 9** shows the cycling stability for cathodes pyrolyzed at 450 °C for 48 h. The initial specific discharge capacity for a Li-based  $\text{TiS}_{2-x}$  system is 217  $\text{mAh g}^{-1}$  (**Figure 9A**). The second cycle exhibits a discharge capacity of 221  $\text{mAh g}^{-1}$  which is equivalent to an energy density of 433  $\text{Wh kg}^{-1}$ . An initial lower discharge capacity followed by a stabilization of the capacity at higher values is quite unusual. Many cathode systems exhibit their highest capacity in the first discharge with an immediate drop in discharge in the second cycle before stabilizing.<sup>32,33</sup> This drop in capacity between the first two discharge cycles is attributed to the growth of an interfacial layer on the surface of the cathode material. This layer is commonly referred to the solid electrolyte interface or to the more recently proposed solid permeable interface.<sup>34</sup> At cycle 10, the discharge capacity of the battery reaches a steady value of 225  $\text{mAh g}^{-1}$ . Over the next 90 cycles, the  $\text{TiS}_2$  cathode shows remarkable robustness with a discharge capacity of 224  $\text{mAh g}^{-1}$  which is translated to Li loading of  $\text{Li}_{0.94}\text{TiS}_{2-x}$  with a capacity retention of 99.5%. This significant discharge capacity retention alludes to the long-term stability of the Li-based  $\text{TiS}_{2-x}$  system.

half-cells were charged/discharged at a 0.1 C rate for 100 cycles. Cathodes were pyrolyzed at 450 °C for 48 h.

When discharged at a 0.1 C rate, Na-based  $\text{TiS}_{2-x}$  half-cells, on the other hand, yield an initial specific discharge capacity of  $\approx 217 \text{mAh g}^{-1}$  (**Figure 9B**). This specific discharge capacity is equivalent to a Na loading of  $\text{Na}_{0.91}\text{TiS}_2$ . This loading is higher than that reported as the top limit of only 0.8 Na-ions per  $\text{TiS}_2$  unit.<sup>47, 66</sup> Although we do not observe any initial irregularities in the discharge capacity upon cycling the Na-based  $\text{TiS}_2$  half-cells, their long-term stability is not as robust as that observed for the Li-based  $\text{TiS}_{2-x}$  system. Over 100 cycles, 89.7% of the initial specific discharge capacity is maintained. Also, upon cycling, the specific discharge capacity does not fall below the 0.8 Na-ions per  $\text{TiS}_2$  unit value of 191.2  $\text{mAh g}^{-1}$ . This specific capacity is equivalent to an energy density of 372  $\text{Wh kg}^{-1}$ . It is important to note that previous studies on  $\text{TiS}_2$  have predominantly focused on elucidating the electrochemical properties of bulk platelets with micron-sized dimensions. Diffusion of the Na-ion into the center of these platelets likely becomes energetically unfavorable. However, by reducing the dimensionality of individual  $\text{TiS}_2$  nanobelts as well as the fabrication of a well-defined hierarchical structure, the diffusion length to the middle of the nanobelt may be significantly reduced. In addition, the nanoscale morphology allows for greater lattice expansion without fracturing the crystal lattice.

To further investigate the role that Li- and Na- ion diffusion has on the electrochemical performance of our vertically oriented  $\text{TiS}_x$  nanobelt arrays, GITT studies were performed. As described by Weppner and Huggins, GITT combines both transient and steady-state measurements to study the kinetic properties of an electrode.<sup>67</sup> During GITT analysis, the coin cells are subjected to a short pulse of fixed current and the voltage response is measured as a function of time. The coin cells are then allowed to rest for a length of time until the current reaches steady-state. Once steady-state (cutoff limit) is reached, a current pulse is again applied to the coin cells. **Figure 10** shows the GITT discharge curves for both Li- and Na- based  $\text{TiS}_{2-x}$  systems. Here, a 0.1 C current was applied for 60 seconds and then the coin cells were allowed to rest for 2 hours. From the GITT measurements, the diffusion of the Li-ion or Na-ion into the  $\text{TiS}_{2-x}$  matrix host can be calculated according to the following equation:

$$D = \frac{4}{\tau} \left( \frac{I V_M}{n F S} \right)^2 \left[ \frac{\left( \frac{dE}{dx} \right)}{\frac{dE}{d\sqrt{t}}} \right]^2 \quad (4)$$

where  $D$  is the  $\text{Li}^+$  or  $\text{Na}^+$  ion diffusion coefficient,  $I$  is the applied current pulse,  $n$  is the number of electrons involved during ion diffusion ( $n = 1$  for both  $\text{Li}^+$  and  $\text{Na}^+$ ),  $F$  is the Faraday constant,  $S$  is the electrode/electrolyte contact area ( $5.4 \text{ m}^2 \text{g}^{-1}$  for vertically oriented  $\text{TiS}_2$  nanobelt arrays,

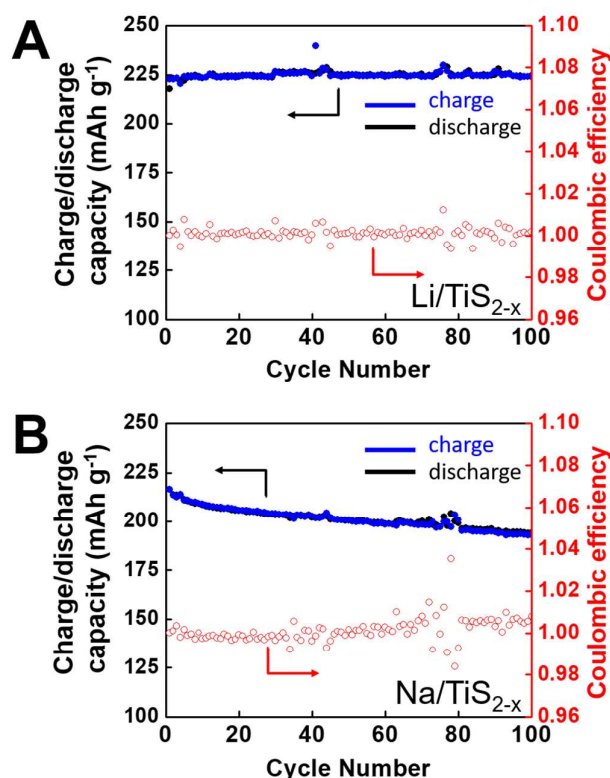


**Figure 9.** Cycling performance and Coulombic efficiency for a half-cell comprising vertically oriented  $\text{TiS}_{2-x}$  cathodes. The

determined from  $N_2$  adsorption-desorption experiments),  $V_M$  is the molar volume of the vertically oriented  $TiS_{2-x}$  nanobelt arrays,  $x$  is the loading of the Li or Na in the cathode material ( $Li_xTiS_{2-x}$  and  $Na_xTiS_{2-x}$ ), and  $\tau$  is the current pulse time. The value for  $dE/dx$  is obtained by measuring the change in the equilibrium electrode potential after each current pulse. The value  $dE/dvt$  is determined from the voltage response plotted against the square root of the time during each current pulse. As depicted in **Figure 10A**, a GITT capacity of  $238 \text{ mAh g}^{-1}$  is obtained in the first charge/discharge cycle for the Li-based  $TiS_2$  half-cell. This GITT capacity is slightly higher than the one obtained from the galvanostatic measurements (**Figure 8 and 9**). Such discrepancy is due to the equilibration of the half-cell prior to applying a current pulse (the cell equilibration is also observed in the Na-based  $TiS_{2-x}$  system, *vide infra*). The log diffusion coefficients ( $D$ ) of  $Li^+$  into the vertically oriented  $TiS_{2-x}$  nanobelt array cathode insertion host, as calculated by employing GITT are also presented in **Figure 10A**. Here, the log diffusion coefficients for the Li-ion upon being inserted into the  $TiS_{2-x}$  cathode show a rapid decrease at lower specific capacities followed by an increase in diffusion rate between  $20 - 200 \text{ mAh g}^{-1}$ .

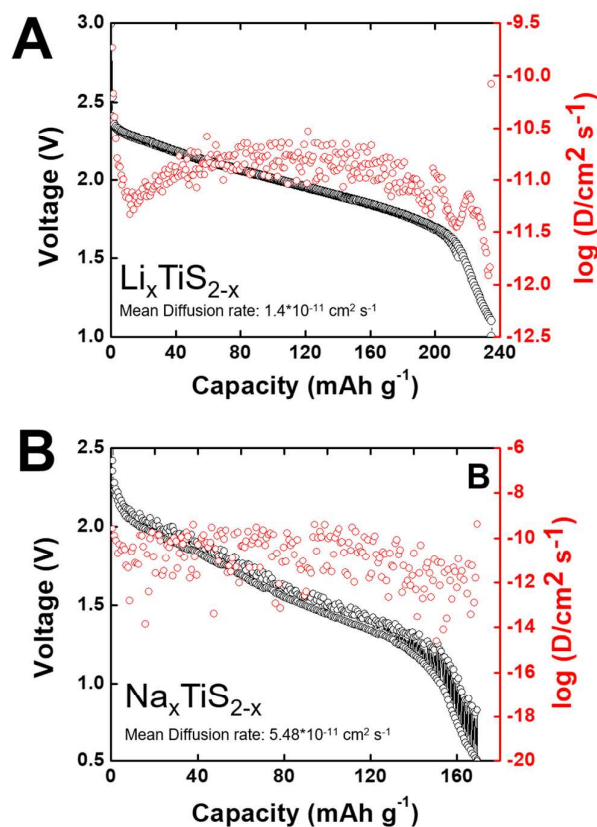


**Figure 10.** Galvanostatic intermittent titration technique (GITT) curves for Li- (A) and Na- (B) based  $TiS_2$  half-cells.

Finally, we observe a decrease in the diffusion rate as the cathode became fully intercalated ( $238 \text{ mAh g}^{-1}$ ). Using the

slope of the transient-voltage GITT curve ( $dE/dx$ ) and the slope of the equilibrium voltage ( $dE/dvt$ ), we calculate a mean diffusion rate of  $1.4 \times 10^{-11} \text{ cm}^2 \text{ s}^{-1}$  for the Li-ions intercalated into our vertically oriented  $TiS_{2-x}$  cathode insertion hosts. The calculated mean diffusion rate is on par with previously reported values for  $Li^+$  diffusion in layered  $TiS_2$  and cubic  $Ti_2S_4$  electrodes.<sup>68, 69</sup> In contrast, the log diffusion coefficient of the Na-ion into the vertically oriented  $TiS_2$  cathode shows a steadier trend (**Figure 10B**). However, there is greater variance in the diffusion rates. The mean diffusion rate for the intercalation of Na-ions into the  $TiS_{2-x}$  cathode is calculated to be  $5.5 \times 10^{-11} \text{ cm}^2 \text{ s}^{-1}$ , which is comparable to previous reports using  $TiS_2$  nanoplates as the electrode.<sup>48</sup> Thus by increasing the surface area of the electrode upon reducing its size to the nanoscale regime as well as the fabrication of anisotropic structures strongly favor Li(Na) insertion into the  $TiS_{2-x}$  cathode with the advantage of having a highly conducting matrix host that does not require the addition of a binder or a conductive additive.

## Conclusions

In summary, we present the synthesis and electrochemical characterization of vertically oriented  $TiS_{2-x}$  nanobelt arrays. These highly anisotropic structures serve as binder- and carbon-free cathode insertion hosts for Li- and Na-ion energy storage devices. The control of the spatial geometry as well as the amount of sulfur vacancies present in the  $TiS_{2-x}$  nanobelt arrays enable high rate electrochemical performances and high stabilities for both  $Li^+$  and  $Na^+$  insertion. We believe that the direct growth of vertically oriented  $TiS_2$  nanobelt arrays onto the current collector as well as the increased electrode/electrolyte surface contact area suppress the uncontrollable growth of an SEI layer and allow high Li (Na) diffusion coefficients. As a result, our vertically oriented  $TiS_2$  nanobelt arrays, when used as cathode insertion hosts deliver high and stable capacities without the need of any additives. Our findings provide fundamental insights for guiding the rational design of other highly anisotropic metal chalcogenide energy storage materials that could serve as binder- and carbon-free cathode (anode) insertion hosts for both monovalent and heterovalent energy storage devices.

## Conflicts of interest

There are no conflicts to declare.

## Acknowledgements

This work was supported by the NSF MRSEC program at the Univ. of Utah under Grant No. DMR 1121252. C.G.H. acknowledges funding from the Utah Governor's Office of Energy Development. L.W.B. would also like to acknowledge

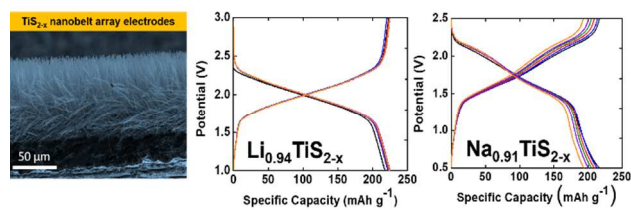
the financial support from the Marion Milligan Mason Award for Women in the Chemical Sciences administered by the American Association for the Advancement of Science and from the Research Corporation for Science Advancement through a Cottrell Scholar Award. The authors gratefully acknowledge Mr. David M. Parker for his help with acquiring the HRTEM data.

## References

- G. E. Blomgren, *J. Electrochem. Soc.*, 2017, **164**, A5019-A5025.
- C. Julien, A. Mauger, A. Vijn and K. Zaghib, in *Lithium Batteries: Science and Technology*, eds. C. Julien, A. Mauger, A. Vijn and K. Zaghib, Springer International Publishing, Cham, 2016, pp. 29-68.
- N. Nitta, F. Wu, J. T. Lee and G. Yushin, *Mater. Today*, 2015, **18**, 252-264.
- A. Elia Giuseppe, K. Marquardt, K. Hoepfner, S. Fantini, R. Lin, E. Knipping, W. Peters, J. F. Drillet, S. Passerini and R. Hahn, *Adv. Mater.*, 2016, **28**, 7564-7579.
- B. Dunn, H. Kamath and J.-M. Tarascon, *Science*, 2011, **334**, 928.
- N. Yabuuchi, K. Kubota, M. Dahbi and S. Komaba, *Chem. Rev.*, 2014, **114**, 11636-11682.
- N. C. and G. S., *Wiley Interdisciplinary Reviews: Energy and Environment*, 2015, **4**, 253-278.
- I. Hasa, D. Buchholz, S. Passerini and J. Hassoun, *ACS Appl. Mater. Interfaces*, 2015, **7**, 5206-5212.
- Q. Zhao, Y. Hu, K. Zhang and J. Chen, *Inorg. Chem.*, 2014, **53**, 9000-9005.
- X. Ren and Y. Wu, *J. Am. Chem. Soc.*, 2013, **135**, 2923-2926.
- D. Aurbach, H. Gizbar, A. Schechter, O. Chusid, H. E. Gottlieb, Y. Gofer and I. Goldberg, *J. Electrochem. Soc.*, 2002, **149**, A115-A121.
- D. Aurbach, Z. Lu, A. Schechter, Y. Gofer, H. Gizbar, R. Turgeman, Y. Cohen, M. Moshkovich and E. Levi, *Nature*, 2000, **407**, 724.
- A. Ponrouch, C. Frontera, F. Bardé and M. R. Palacin, *Nat. Mater.*, 2015, **15**, 169.
- S. K. A., G. J. A., J. Young, Si, W. Fred, S. G. D. and S. Ram, *Adv. Energy Mater.*, 2013, **3**, 1056-1061.
- M.-C. Lin, M. Gong, B. Lu, Y. Wu, D.-Y. Wang, M. Guan, M. Angell, C. Chen, J. Yang, B.-J. Hwang and H. Dai, *Nature*, 2015, **520**, 324.
- H. Sun, W. Wang, Z. Yu, Y. Yuan, S. Wang and S. Jiao, *Chem. Commun.* 2015, **51**, 11892-11895.
- E. I. Shkolnikov, A. Z. Zhuk and M. S. Vlaskin, *Renewable and Sustainable Energy Rev.*, 2011, **15**, 4611-4623.
- Q. Li and N. J. Bjerrum, *J. Power Sources*, 2002, **110**, 1-10.
- D. A. Stevens and J. R. Dahn, *J. Electrochem. Soc.*, 2001, **148**, A803-A811.
- Y. Wang, R. Xiao, Y.-S. Hu, M. Avdeev and L. Chen, *Nat. Commun.*, 2015, **6**, 6954.
- J. Sun, H.-W. Lee, M. Pasta, H. Yuan, G. Zheng, Y. Sun, Y. Li and Y. Cui, *Nat. Nanotechnol.*, 2015, **10**, 980.
- X. Xia and J. R. Dahn, *Electrochem. Solid-State Lett.*, 2011, **15**, A1-A4.
- M. Sathiya, K. Hemalatha, K. Ramesha, J. M. Tarascon and A. S. Prakash, *Chem. Mater.*, 2012, **24**, 1846-1853.
- N. Yabuuchi, M. Kajiyama, J. Iwatate, H. Nishikawa, S. Hitomi, R. Okuyama, R. Usui, Y. Yamada and S. Komaba, *Nat. Mater.* 2012, **11**, 512.
- D. W. Han, J. H. Ku, R. H. Kim, D. J. Yun, S. S. Lee and S. G. Doo, *ChemSusChem*, 2014, **7**, 1870-1875.
- X. Kong, T. Zhu, F. Cheng, M. Zhu, X. Cao, S. Liang, G. Cao and A. Pan, *ACS Appl. Mater. Interfaces* 2018, **10**, 8730-8738.
- K. T. Lee, T. N. Ramesh, F. Nan, G. Botton and L. F. Nazar, *Chem. Mater.*, 2011, **23**, 3593-3600.
- P. Moreau, D. Guyomard, J. Gaubicher and F. Boucher, *Chem. Mater.*, 2010, **22**, 4126-4128.
- Y. Fang, J. Zhang, L. Xiao, X. Ai, Y. Cao and H. Yang, *Adv. Sci.*, 2017, **4**, 1600392.
- F. Wang, S.-W. Kim, D.-H. Seo, K. Kang, L. Wang, D. Su, J. J. Vajo, J. Wang and J. Graetz, *Nat. Commun.*, 2015, **6**, 6668.
- D. Deng, *ChemNanoMat*, 2016, **3**, 146-159.
- L. P. Wang, L. Yu, X. Wang, M. Srinivasan and Z. J. Xu, *J. Mater. Chem. A*, 2015, **3**, 9353-9378.
- X. Wang, D. Chen, Z. Yang, X. Zhang, C. Wang, J. Chen, X. Zhang and M. Xue, *Adv. Mater.*, 2016, **28**, 8645-8650.
- E. Yang, H. Ji and Y. Jung, *J. Phys. Chem. C*, 2015, **119**, 26374-26380.
- J. S. Cho, S. Y. Lee and Y. C. Kang, *Sci. Rep.*, 2016, **6**, 23338.
- I.-H. Chu, C. S. Kompella, H. Nguyen, Z. Zhu, S. Hy, Z. Deng, Y. S. Meng and S. P. Ong, *Sci. Rep.*, 2016, **6**, 33733.
- W. Luo, A. Calas, C. Tang, F. Li, L. Zhou and L. Mai, *ACS Appl. Mater. Interfaces*, 2016, **8**, 35219-35226.
- B. Huang, Y. I. Jang, Y. M. Chiang and D. R. Sadoway, *J. Appl. Electrochem.*, 1998, **28**, 1365-1369.
- A. Zhou, J. Xu, X. Dai, B. Yang, Y. Lu, L. Wang, C. Fan and J. Li, *J. Power Sources*, 2016, **322**, 10-16.
- C. Wan, X. Gu, F. Dang, T. Itoh, Y. Wang, H. Sasaki, M. Kondo, K. Koga, K. Yabuki, G. J. Snyder, R. Yang and K. Koumoto, *Nat. Mater.*, 2015, **14**, 622.
- S.-H. Chung, L. Luo and A. Manthiram, *ACS Energy Lett.*, 2018, **3**, 568-573.
- L. Wang, J. Zou, S. Chen, G. Zhou, J. Bai, P. Gao, Y. Wang, X. Yu, J. Li, Y.-S. Hu and H. Li, *Energy Storage Mater.*, 2018, **12**, 216-222.
- L. Ma, S. Wei, H. L. Zhuang, K. E. Hendrickson, R. G. Hennig and L. A. Archer, *J. Mater. Chem. A*, 2015, **3**, 19857-19866.
- D. Y. Oh, Y. E. Choi, D. H. Kim, Y.-G. Lee, B.-S. Kim, J. Park, H. Sohn and Y. S. Jung, *J. Mater. Chem. A*, 2016, **4**, 10329-10335.
- K. Sun, Q. Zhang, D. C. Bock, X. Tong, D. Su, A. C. Marschillok, K. J. Takeuchi, E. S. Takeuchi and H. Gan, *J. Electrochem. Soc.*, 2017, **164**, A1291-A1297.
- M. S. Whittingham, *Science*, 1976, **192**, 1126.
- G. H. Newman and L. P. Klemann, *J. Electrochem. Soc.*, 1980, **127**, 2097-2099.
- Y. Liu, H. Wang, L. Cheng, N. Han, F. Zhao, P. Li, C. Jin and Y. Li, *Nano Energy*, 2016, **20**, 168-175.
- T. Eriksson, A. M. Andersson, C. Gejke, T. Gustafsson and J. O. Thomas, *Langmuir*, 2002, **18**, 3609-3619.
- L. Bao, L. Li, G. Xu, J. Wang, R. Zhao, G. Shen, G. Han and S. Zhou, *Electrochim. Acta*, 2016, **222**, 685-692.
- N. Böckenfeld and A. Balducci, *J. Appl. Electrochem.*, 2014, **44**, 467-474.
- C. G. Hawkins and L. Whittaker-Brooks, *ACS Appl. Nano Mater.*, 2018, **1**, 851-859.

53. J. O. Island, R. Biele, M. Barawi, J. M. Clamagirand, J. R. Ares, C. Sánchez, H. S. J. van der Zant, I. J. Ferrer, R. D'Agosta and A. Castellanos-Gomez, *Sci. Rep.*, 2016, **6**, 22214.
54. M. H. Lindic, H. Martinez, A. Benayad, B. Pecquenard, P. Vinatier, A. Levasseur and D. Gonbeau, *Solid State Ionics*, 2005, **176**, 1529-1537.
55. M. S. Whittingham, *Dalton Trans.*, 2008, 5424-5431.
56. A. S. Aricò, P. Bruce, B. Scrosati, J.-M. Tarascon and W. van Schalkwijk, *Nat. Mater.* 2005, **4**, 366.
57. H.-C. Wu, H.-C. Wu, E. Lee and N.-L. Wu, *Electrochem. Commun.*, 2010, **12**, 488-491.
58. I. Doberdò, N. Löffler, N. Laszczynski, D. Cericola, N. Penazzi, S. Bodoardo, G.-T. Kim and S. Passerini, *J. Power Sources*, 2014, **248**, 1000-1006.
59. M. E. Fleet, S. L. Harmer, X. Liu and H. W. Nesbitt, *Surf. Sci.*, 2005, **584**, 133-145.
60. J. Benard and Y. Jeannin, in *Nonstoichiometric Compounds*, J. Am. Chem. Soc., 1963, pp. 191-203.
61. A. H. Thompson, F. R. Gamble and C. R. Symon, *Mater. Res. Bull.*, 1975, **10**, 915-919.
62. S. Gutmann, M. A. Wolak, M. Conrad, M. M. Beerbom and R. Schlaf, *J. Appl. Phys.*, 2010, **107**, 103705.
63. S. Krischok, J. Günster, D. W. Goodman, O. Höfft and V. Kempter, *Surf. Interface Anal.*, 2005, **37**, 77-82.
64. C. Jun, T. Zhan-Liang and L. Suo-Long, *Angew. Chem. Int. Ed.*, 2003, **42**, 2147-2151.
65. J. Kasnatscheew, U. Rodehorst, B. Streipert, S. Wiemers-Meyer, R. Jakelski, R. Wagner, I. C. Laskovic and M. Winter, *J. Electrochem. Soc.*, 2016, **163**, A2943-A2950.
66. B. G. Silbernagel and M. S. Whittingham, *Mater. Res. Bull.*, 1976, **11**, 29-36.
67. W. Weppner and R. A. Huggins, *J. Electrochem. Soc.*, 1978, **124**, 1569-1578.
68. A. J. Vaccaro, T. Palanisamy, R. L. Kerr and J. T. Maloy, *Solid State Ionics*, 1981, **2**, 337-340.
69. A. C. W. P. James, J. B. Goodenough and N. J. Clayden, *J. Solid State Chem.*, 1988, **77**, 356-365.

## TOC



Vertically-oriented  $\text{TiS}_2$  nanobelt arrays allow for the fabrication of carbon- and binder- free electrodes with high ion diffusion lengths.